processes

MDPI

Article

Modal Analysis on MVG Controlled Supersonic Flow at Different Mach Numbers

Yong Yang [1], Yonghua Yan [2,*], Caixia Chen [3], Qingquan Wu [1], Tor A. Kwembe [2] and Ryan Wu [2]

[1] Department of Mathematics, West Texas A&M University, Canyon, TX 79016, USA; yyang@wtamu.edu (Y.Y.); qwu@wtamu.edu (Q.W.)
[2] Department of Mathematics & Statistical Sciences, Jackson State University, Jackson, MI 39217, USA; tor.a.kwembe@jsums.edu (T.A.K.); ryanboydwu@yahoo.com (R.W.)
[3] Department of Mathematics and Computer Science, Tougaloo College, Tougaloo, MI 39174, USA; cchen1@tougaloo.edu
* Correspondence: yonghua.yan@jsums.edu

Abstract: Modal analysis on micro-vortex generator (MVG)-controlled supersonic flow at different Mach numbers is performed in this paper. The purpose of this investigation is to clarify the different properties of streamwise and ring-like vortical modes, and the effects of different Mach numbers on these modes, to further understand the vortical structures as they travel from MVG down to the shock wave/boundary-layer interaction (SWBLI) region. To this end, a high order and high resolution large eddy simulation (LES) was carried out, which identified the vortical structures behind the MVG and in the shock wave/boundary-layer interaction (SWBLI) region in the supersonic ramp flow with flow speeds of three different Mach numbers 1.5, 2.0, and 2.5. The proper orthogonal decomposition (POD) then was adopted to investigate the modes of the fluctuation flow field. It emerged that the streamwise and ring-like vortical modes were disparate in energy distribution, structural order, frequency and amplitude. Furthermore, it showed that as the Mach number increased, the energy of the streamwise modes increased while the opposite was true for ring-like modes; and the streamwise modal structures were altered more significantly than the ring-like modes, and the frequency of each mode scarcely varied. It was also found that the streamwise vortices absorbed energy from the ring-like vortices while they traveled from the MVG down to the SWBLI region, but the dominant frequency of each mode rarely changed during this process.

Keywords: LES; MVG; SWBLI; POD

Citation: Yang, Y.; Yan, Y.; Chen, C.; Wu, Q.; Kwembe, T.A.; Wu, R. Modal Analysis on MVG Controlled Supersonic Flow at Different Mach Numbers. *Processes* **2022**, *10*, 1456. https://doi.org/10.3390/pr10081456

Academic Editor: Alessandro D' Adamo

Received: 1 July 2022
Accepted: 22 July 2022
Published: 25 July 2022

1. Introduction

The shock wave/boundary-layer interaction (SWBLI) has remained an unsolved phenomenon in aerodynamics for many years, due to its complexity. It reduces flow quality by inducing large-scale flow separation, which can significantly decrease aircraft and engine performance. This often results in undesirable effects such as total pressure loss, unstable engine flow, increased engine drag and high wall heating. To reduce the adverse effects caused by SWBLI, the micro vortex generator (MVG) is a simple and reliable device that induces separation control. MVGs are passive control devices that are smaller (below the thickness of the supersonic boundary layer) than conventional vortex generators used for low-speed flow control. Due to this small size, MVGs can sustain much lower drag losses while mitigating flow separation [1–6].

In the last decade, experiments and computational investigations on MVGs have been carried out. Babinsky et al. [2] performed a series of experiments on different MVGs and created a detailed study on their control effects. Sun et al. [7] made a PIV investigation of the 3D instantaneous flow organization behind a micro-ramp in a supersonic boundary layer, and Wang et al. [8] performed an NPLS and PIV experimental study in a low-noise supersonic wind-tunnel. Numerical simulations have been made on MVGs for comparative studies and further design, using RANS, hybrid RANS/LES, and monotone integrated LES. Rizzetta and Visbal [9] simulated the flow field on a compression corner by implicit LES using a high-order method. Von Kaenal et al. [10] used an approximate de-convolution model to conduct the LES on ramp flow. Ghosh et al. [11] conducted numerical simulations using RANS and hybrid LES/RANs under the conditions of Babinsky's experiment [2]. Similar fundamental flow structures, such as the streamwise vortices and momentum deficit, were reproduced. Lee et al. [12] adopted monotone integrated large eddy simulations to simulate the MVG controlled supersonic flow and reported the fundamental wave system generated by MVG-including the main shock, expansion waves and recompression shocks. Lee et al. [13] further tested several variations of the standard MVG and micro vane to optimize the control effect. John [14,15] extended the FLASH code to enable simulation on high-speed compressible viscous flow past arbitrary two- and three-dimensional stationary bodies. The computed results have been found to be consistent with experimental results. Zhang et al. [16] investigated the induced velocity and the trajectory of the vortices generated by MVGs by using the point vortex model and the effect of the asymmetric micro-ramp was numerically studied at a free stream Mach number of 2.5 via RANS simulations. For the optimization of MVG, Said [17] studied the effect of the streamwise location of an MVG on the aerodynamic performance on airfoils in subsonic flow. Khare et al. [18] studied the effect of MVG width on characteristics of the primary vortex. The results from four case with different MVG width were obtained and compared.

In our previous work [19–21], we performed numerical simulations of supersonic ramp flow with MVG control at $Ma = 2.5$ and $Re = 5760$ to understand the flow structures, especially the 3D vortex structures, behind the MVG. From our data, a dynamic vortex model was provided. The results of our LES also revealed a series of ring-like (or Ω shaped) vortices [20] behind MVGs that traveled downstream. Furthermore, the shock waves at the ramp corner were weakened substantially when interacted with the boundary layer that contained ring-like vortices at the upper bound [21].

In this paper, a proper orthogonal decomposition (POD) method [22] combined with vortex visualization was used to study the flow structure in SWBLI. POD can extract information from snapshots of the flow field based on approximations produced by projecting high-dimensional matrices into low-dimensional subspaces. It determines the most energetic (significant) structures by diagonalizing the spatial correlation matrix computed from the snapshots, based on the energy ordering of orthogonal structures in the matrix.

The structure of this paper is as follows: Section 2 briefly introduces the numerical method used in this study, including the analytical method used-POD, Section 3 briefly introduces the flow structure visualized in the numerical results, the POD analysis results, including mode energy. The distribution, model vortex structure, and model time coefficients are given in Section 4; the conclusions are summarized in Section 5.

2. Case Setup and Numerical Methods

2.1. Case Setup

In this study, supersonic ramp flow with an MVG installed on the wall boundary of the upstream domain was investigated. Figure 1a is a schematic diagram of the flow field. This study reconstructed a fully developed turbulent inflow at supersonic speeds as the inflow. This study had a boundary layer thickness set to twice the height of the MVG, generated in front of the MVG. In supersonic ramp flows, ramp shocks (or separation shocks in the figure) induce large separation regions. Figure 1b shows the dimensions of the ramp and the location of the MVG in the domain. The grid size of the entire system was $nspanwise \times nnormal \times nstreamwise = 137 \times 192 \times 1600$. The horizontal distance from MVG tip to the ramp corner was $19.5\ h$. The distance from the end of the ramp to the MVG tip was about $32.29\ h$. The distance between the inlet and the MVG tip was

17.78 h. Figure 2 shows the grids around the MVG on a streamwise central plane, the grids were refined at the wall boundary. More detailed dimensions of the MVG and computational domain can be found in [20].

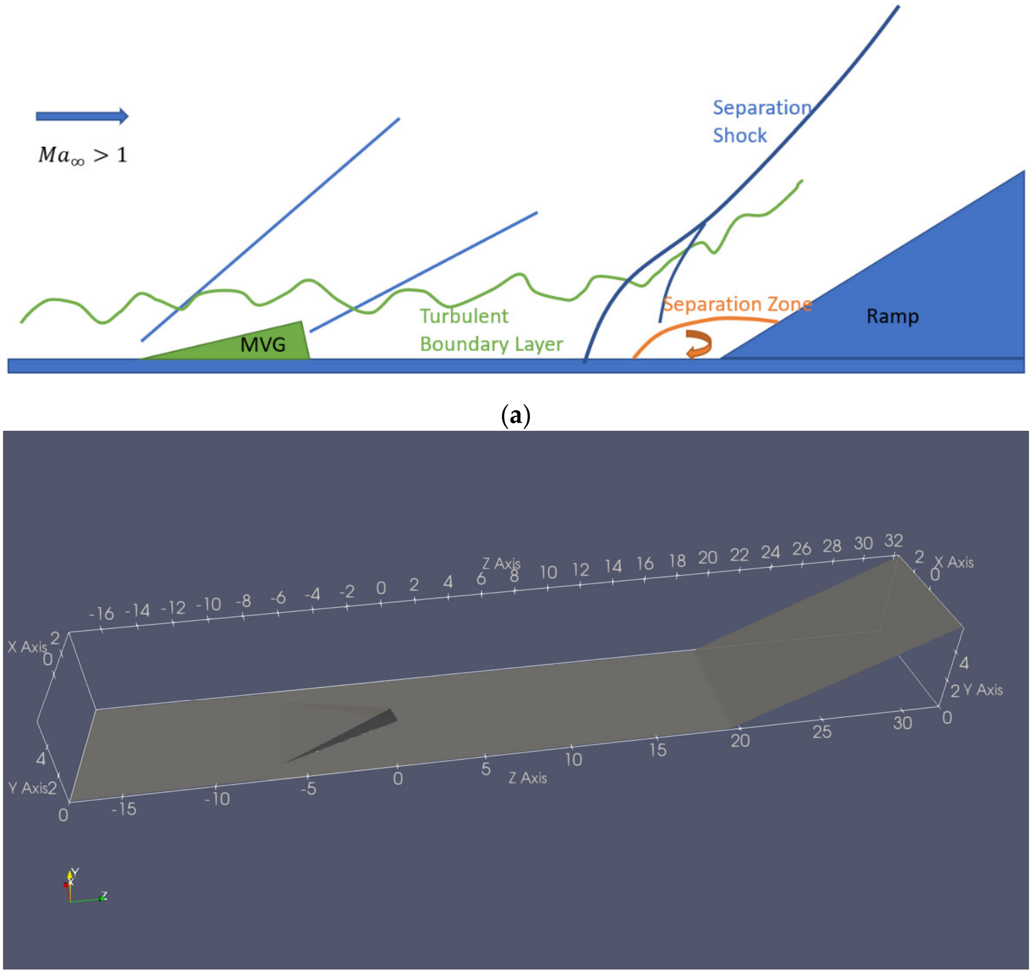

(**a**)

(**b**)

Figure 1. The illustration of the flow field (**a**) and the domain with MVG installed on the wall boundary (**b**).

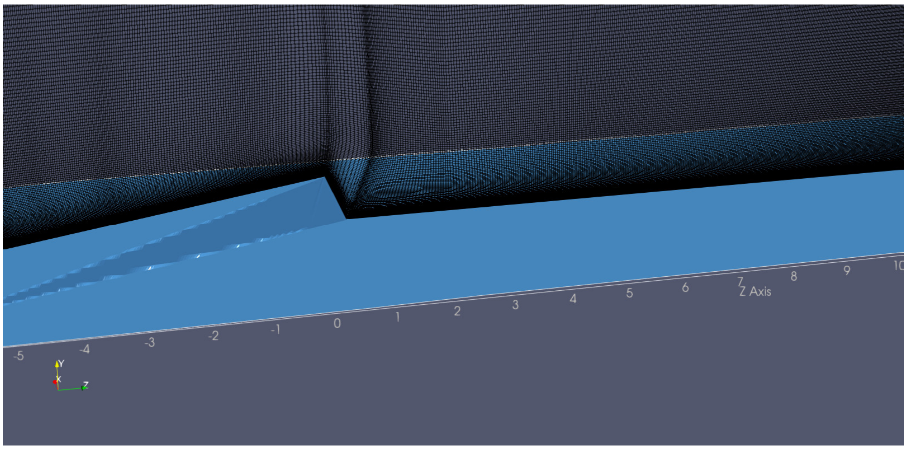

Figure 2. Grids around the tip of MVG.

Our inhouse monotone integrated LES (MILES) code was adopted by solving the Navier-Stokes using the fifth order bandwidth-optimized WENO scheme [23]. The LES code was previously validated for unsteady supersonic benchmark flows and a MVG controlling ramp flow at $Ma = 2.5$ and $Re = 5760$. The code validations can be found in ref. [20].

The adiabatic, zero-gradient pressure and non-slipping conditions were adopted for the wall boundary condition. To avoid the reflection in the flow field domain, the non-reflecting boundary condition is used for the spanwise, upper and outlet flow boundaries [21].

To mimic the fully developed turbulent inflow, twenty thousand consecutive turbulent profiles were generated in our previous DNS on transition flow [24] and imported into this LES as the inlet condition [19]. After a short range of development, the inflows generated upstream of the MVG were fully developed turbulent flows. In our previous paper [20], the flow properties were also checked and confirmed that a fully developed turbulence flow was obtained in front of the MVG. In this study, three simulations with Mach numbers 1.5, 2.0, and 2.5 were conducted. In all three cases, the boundary layer thickness was consistent in the upstream inlet, which was equivalent to twice the MVG's height (2 h). In addition, the explicit third-order TVD-type Runge-Kutta scheme was employed in time marching.

2.2. Numerical Methods

In this study, the Navier-Stokes equations are solved to simulate the fluid flow. Given the density of the fluid ρ, the momentum $\rho\boldsymbol{u}$, the total energy E at a position $\boldsymbol{x}$ and at time t, the Navier-Stokes equations can be derived as follows from the conservation laws of mass, momentum and energy:

$$\frac{\partial \rho}{\partial t} + \nabla \cdot (\rho \boldsymbol{u}) = 0 \tag{1}$$

$$\frac{\partial (\rho \mathbf{u})}{\partial t} + \nabla \cdot (\rho \mathbf{u} \otimes \boldsymbol{u}) = (\nabla \cdot \sigma) \tag{2}$$

$$\frac{\partial (\rho E)}{\partial t} + \nabla \cdot (\rho E)\boldsymbol{u} - \nabla \cdot (k \nabla T) - \nabla \cdot (\sigma \cdot \boldsymbol{u}) = 0 \tag{3}$$

with

$$E = e + \frac{\boldsymbol{u} \cdot \boldsymbol{u}}{2}$$

and

$$\sigma = -\left[p + \frac{2}{3}\mu(\nabla \cdot u)\right]\boldsymbol{I} + \mu[\nabla u + (\nabla u)^T]$$

Here, σ is the internal shear stress, e is the internal energy per unit mass of the fluid, p denotes the pressure, T represents the temperature, k is the thermal conductivity and μ is the dynamic viscosity.

In three dimensions, the system above contains five equations (the conservation of momentum equation becomes three separate equations). Two extra equations are needed to solve the system for the unknown variables ρ, u, p, E and T. These equations are the equation of state, for a thermally perfect gas,

$$p = \rho R T \tag{4}$$

where R is a gas constant, and the equation for internal energy equation,

$$e = C_v T \tag{5}$$

To reveal the MVG's mechanism and gain a deeper understanding of the complex turbulent flow, high-order and high-resolution DNS/LES is necessary.

Considering the semi-discretized form of a one-dimensional hyperbolic equation can be expressed as:

$$\left(\frac{\partial u}{\partial t}\right)_j = -\frac{h_{j+\frac{1}{2}} - h_{j-\frac{1}{2}}}{\Delta x} \tag{6}$$

For the positive flux, the four upwind-biased schemes on four stencils can be given as

$$\begin{cases} h_0^{+\prime} = \frac{1}{3}f_{j-2} - \frac{7}{6}f_{j-1} + \frac{11}{6}f_j \\ h_1^{+\prime} = -\frac{1}{6}f_{j-1} + \frac{1}{3}f_j + \frac{5}{6}f_{j+1} \\ h_2^{+\prime} = \frac{1}{3}f_j + \frac{5}{6}f_{j+1} - \frac{1}{6}f_{j+2} \\ h_3^{+\prime} = \frac{11}{6}f_{j+1} - \frac{7}{6}f_{j+2} + \frac{1}{3}f_{j+3} \end{cases} \tag{7}$$

Third order is obtained for each individual scheme, combining the schemes in Equation (7) linearly gives a 5th order central scheme with the coefficients $\alpha_1 = 0.05, \alpha_2 = 0.45, \alpha_3 = 0.45$ and $\alpha_4 = 0.01$.

To make the scheme robust for discontinuity solutions, the linear coefficients can be replaced with the corresponding nonlinear ones,

$$\omega_i = \frac{b_i}{b_0 + b_1 + b_2 + b_3}$$

$$b_i = \frac{\alpha_i}{(\varepsilon + IS_i)^2}$$

ε is a small quantity (10^{-6}~10^{-10}) to prevent the denominator from being zero, which should be small enough in supersonic problems with shocks. IS_i is the smoothness functions for the stencils.

For the bandwidth-optimized WENO scheme, a further improvement for ω_k by Martin et al. [23] is

$$\omega_i = \begin{cases} \alpha_k & if\ max(TV_k)\,/\,min(TV_k) < 5\ and\ max(TV_k) < 0.2 \\ \omega_i & otherwise \end{cases}$$

where TV_k stands for the total variation on each candidate stencil.

3. Revisiting Proper Orthogonal Decomposition

The proper orthogonal decomposition (POD) is a procedure for extracting a basis from an ensemble of snapshots to project high-dimensional matrices into low-dimensional subspaces while preserving the essential information of the high-dimensional dataset.

As a starting point, the snapshots ($y(t_1), y(t_2), \ldots$, where $y(t_j) \in \mathbb{R}^m$) for different time-steps are simulated numerically and assembled as a $m \times n$ matrix $Y = (y(t_1), y(t_2), \ldots)$. Singular value decomposition (SVD) guarantees $Y = U\Sigma V^T$. The proper orthonormal basis, or the POD basis, is taken as $\psi_i = U_i, i = 1, \ldots, N$, where U_i denotes the i-th column of U and N is the dimension of the low-dimension subspace.

The snapshots can be approximated by $y(t_j) \approx \sum_{i=1}^{N} a_i(j)\,\psi_i$, where $a_i(j) = \langle \psi_i, y_j \rangle_{\mathbb{R}^m}$ is the time coefficient of each POD-basis and $\langle \cdot, \cdot \rangle_{\mathbb{R}^m}$ denotes the canonical inner product in $\mathbb{R}^m$. We denote $M_{i,j} = a_i(j)\,\psi_i$ as the i-th mode of snapshot $y(t_j)$.

4. Flow Structures from the Numerical Solution

To better capture and understand the vortex structures in the flow field, a novel vortex identification method, Rortex/Liutex [25], which can capture both axes and the magnitude of local fluid rotation, is used in this study. Rortex/Liutex uses RS decomposition to separate non-dissipative rigid rotation from dissipative shear as shown,

$$\vec{\omega} = \vec{R} + \vec{S} \tag{8}$$

$$\vec{R} = \left[(\vec{\omega} \cdot \vec{r}) - \sqrt{(\vec{\omega} \cdot \vec{r})^2 - 4{\lambda_{ci}}^2} \right] \vec{r} \tag{9}$$

where $\vec{r}$ is the real eigenvector of $\nabla \vec{v}$ and $\vec{\omega} \cdot \vec{r} > 0$.

Figure 3 shows the complex vortex structure in the supersonic flow with Ma number 2.5 using the iso-surface of $\|\vec{R}\| = 0.3$ [26]. The ramp shock wave is also presented in Figure 2 using the iso-surfaces of pressure. The large-scale ring-like vortices (see Figure 3) found in our previous work [19,20] are generated at the boundary of a cylindrical momentum deficit shortly behind the MVG. These sturdy ring-like vortices will eventually travel downstream and interact with the strong ramp shock. It is confirmed that these ring-like vortices dominate the SWBLI in the upper boundary layer and are the mechanism of separation zone reductions [20]. Figure 4 shows the transient results for the SWBLI at the ramp corner from all three cases conducted in this study with Ma number 1.5, 2.0 and 2.5. The shock waves (colored gray) in Figure 4 are illustrated by the iso-surface of the gradient of pressure, which can better depict the multi-layer structures of the shock waves than the iso-surfaces of pressure. In all cases, iso-surfaces of gradient pressure are found to be discontinuous where the interaction between the ring-like vortices and ramp shock wave occurs. Moreover, the 3-D ramp shock waves are irregular where the upper boundary layer is located. This indicates that interaction with ring-like vortices substantially distorts and weakens the ramp shock wave.

The process of SWBLI is extremely complicated. This process not only includes the generation, evolution, and energy transfer of various vortices of different scales in the turbulent boundary layer and flow separation zone, but also the impact caused by the strong discontinuity of shock waves. Nonetheless, in-depth exploration of the movement and development of the vortex structure is key to understanding SWBLI. Since the shape and distribution of vortices in the turbulent boundary layer cannot be fully demonstrated by simple visualization methods, the POD method [22], which can determine the most energetic structures, is a particularly valuable tool.

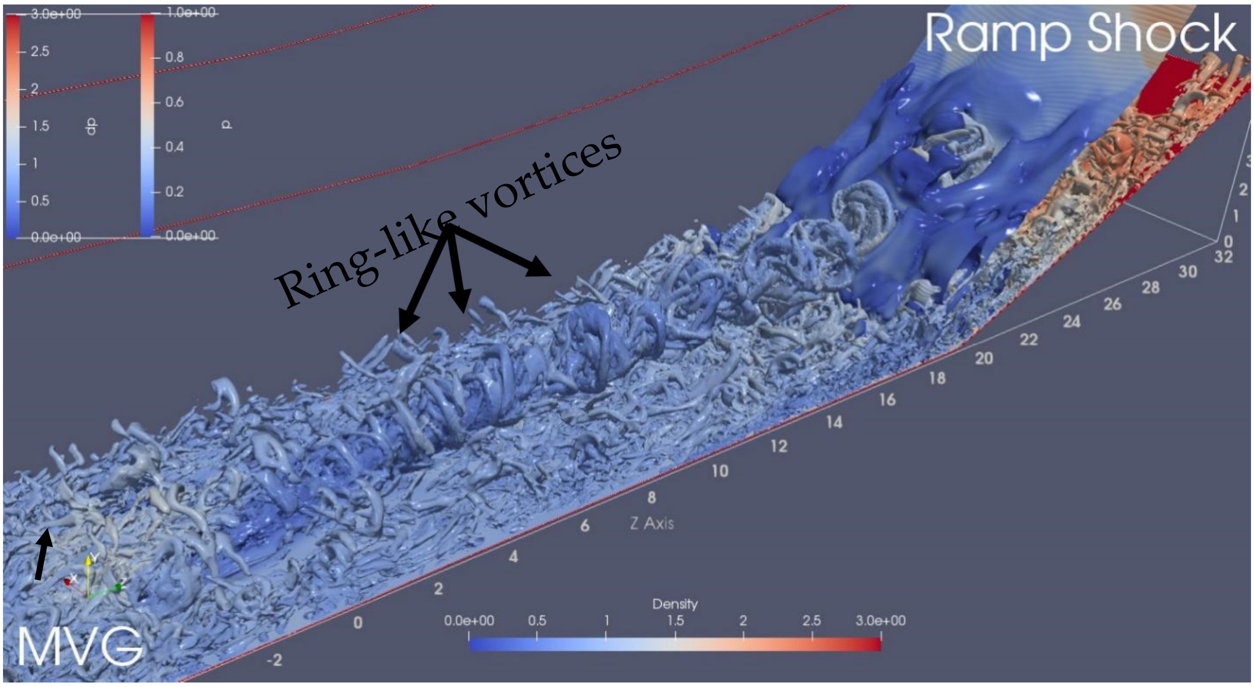

Figure 3. Vortex structure and ramp shock wave (Ma 2.5).

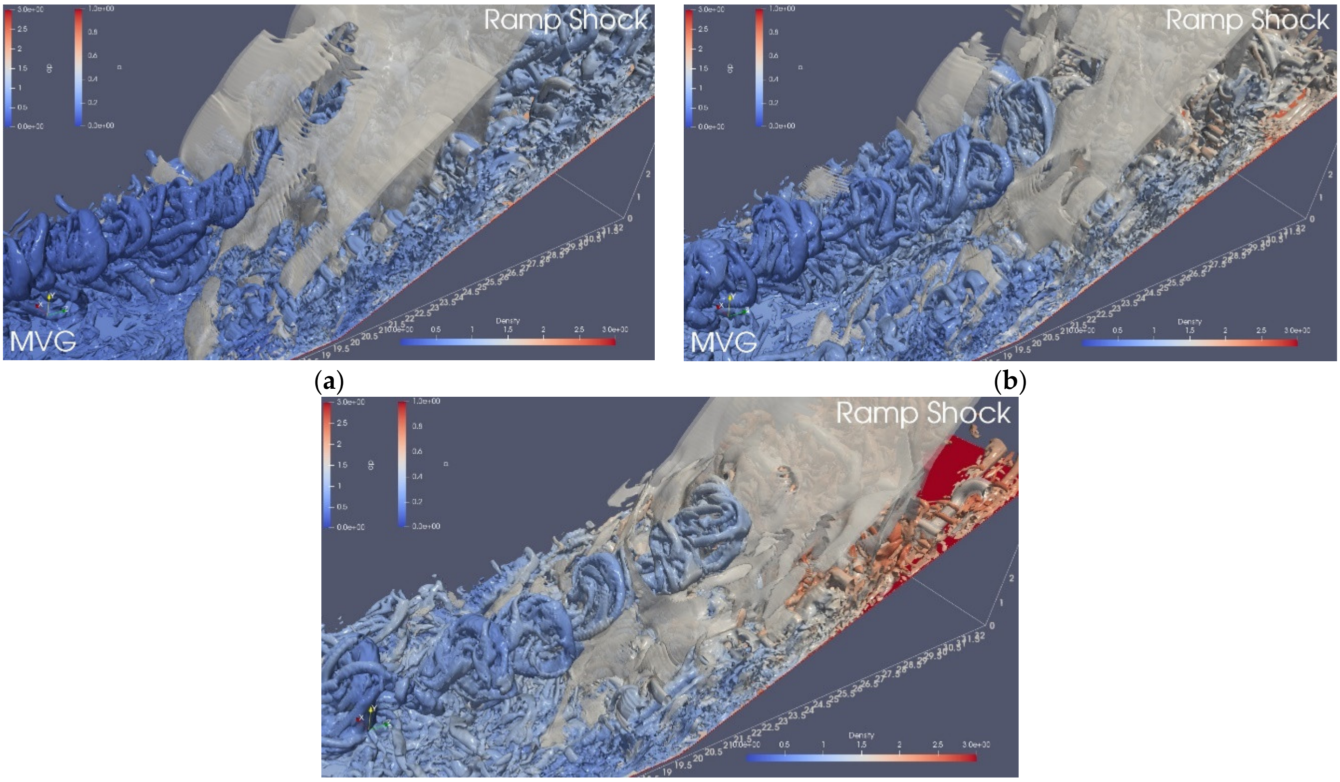

(**a**) (**b**)

(**c**)

Figure 4. SWBLI at the ramp corner (**a**) Ma 1.5 (**b**) Ma 2.0 (**c**) Ma 2.5.

5. POD Analysis on Ring-like Vortical Structures

To investigate the principal components of these vortical structures, we applied POD over 100 snapshots of the fluctuation field in SWBLI. These snapshots came from 50,000 time steps of instantaneous flow data continuously recorded from our numerical simulation. To study the process of SWBLI and its influence on large scale ring-like vortices, two subzones were extracted. One was close behind the MVG, and the other was in the SWBLI region (see Figure 5). These subzones included the upper zones of the turbulent boundary layer, where ring-like vortices mainly exist. The sizes of the subzones were also large enough to capture all the ring-like vortices behind the MVG and in the interaction region with the ramp shock wave.

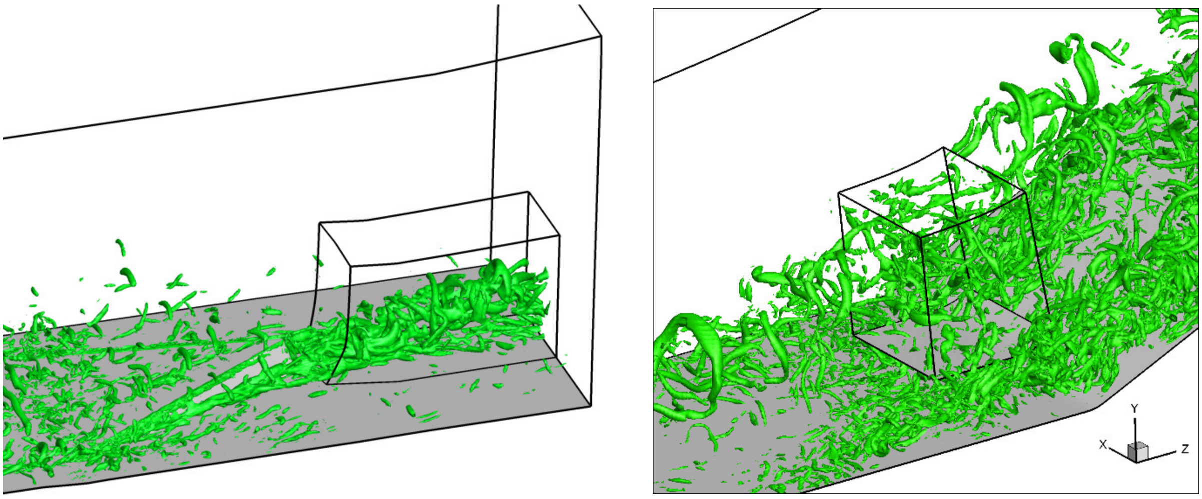

(**a**) (**b**)

Figure 5. Vortical structures and the position of subzones: (**a**) behind the MVG, (**b**) in SWBLI region.

The POD analysis was based on the information obtained from all the snapshots of the two subzones. The matrix Y for each subzone contained 100 snapshots $y(t_j)$ as its columns. Each snapshot $y(t_j)$ was the flattened 1D arrays generated by the raveling of the 3D Rortex/Liutex field, as demonstrated in Figure 6.

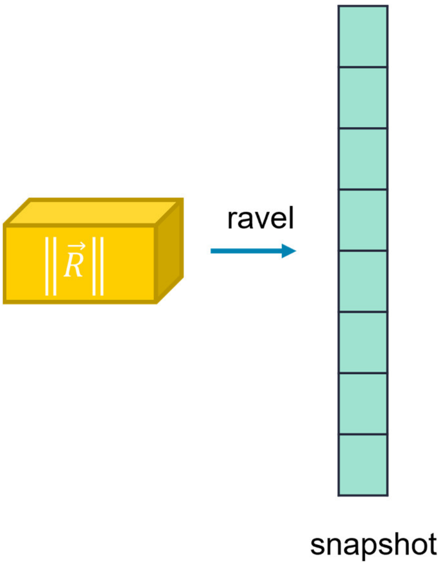

Figure 6. Raveling 3D $\|\vec{R}\|$ field to 1D array.

5.1. POD Analysis behind the MVG

5.1.1. Mode Energy Distribution

Figure 7 shows $\mathcal{E}(\ell)$, the ratio of the modeled to the total energy contained in the system Y, in the subzone behind the MVG in three different Mach numbers. The ratio $\mathcal{E}(\ell)$ is defined as

$$\mathcal{E}(\ell) = \frac{\sum_{i=1}^{\ell} \lambda_i}{\sum_{i=1}^{d} \lambda_i} \tag{10}$$

where λ_i is the eigenvalues of matrix $Y^T Y$ and $\lambda_i = \sigma_i^2$.

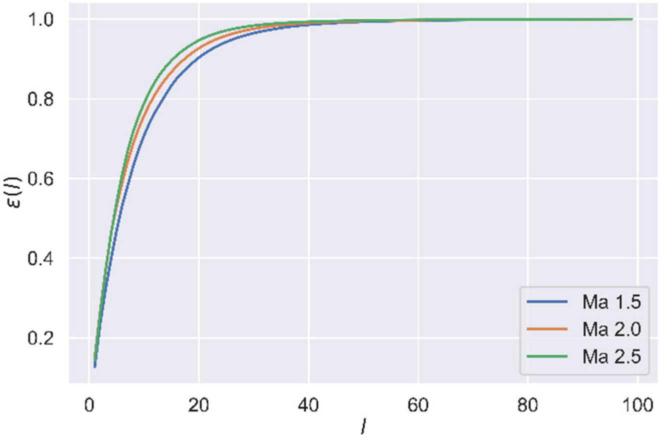

Figure 7. $\mathcal{E}(\ell)$ in the subzone behind the MVG in three different Mach numbers.

From the distribution of $\mathcal{E}(\ell)$, we observe that the first 20 modes recover the snapshots very well. The first 20 modes contributed on average about 90.3, 92.7 and 94.7% of $\mathcal{E}(\ell)$ in the subzone behind the MVG in Ma numbers 1.5, 2.0, and 2.5, respectively. To simplify the aforementioned discussion, the analysis only focused on the first 20 modes.

From Figure 7, we can see that the curve of $\mathcal{E}(\ell)$ was fuller when the Mach number was higher. This was investigated by comparing the energy percentage of the first 20 modes, provided in Figure 8. As the ordinal increased, each mode's contribution rate to the total energy decreased. The energy increased as Mach number increased for the low ordinal modes, but the trend was reversed for the high ordinal modes.

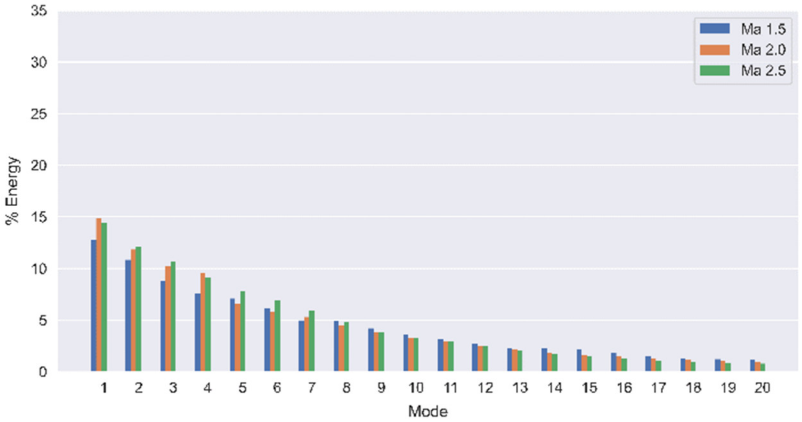

Figure 8. The energy percentage of the first 20 modes behind the MVG in three different Mach numbers.

5.1.2. Mode Vortical Structures

Figure 9 shows the vortical structures of the first 20 modes in the region behind the MVG with Ma 1.5, Ma 2.0, and Ma 2.5, respectively. The vortical structures are indicated by iso-surfaces of $\|\vec{R}\| = 0.3$. From Figure 9, we find that the low ordinal modes had disordered structures, while the high ordinal modes had relatively regular structures, and as the Mach number varied, the vortical structures of low ordinal modes were altered drastically, but the high ordinal modes had more sturdy structures.

Another manifest finding from Figure 9 was that the low ordinal modes (see mode #1, #2, and #3) contributed to the formation of streamwise vortices, and the high ordinal modes (see mode #4–#20, especially mode #11–#20) to ring-like vortices. Combined with the data in Figure 8, the streamwise vortical modes had higher energy, 11.83% on average, and the ring-like vortical modes had lower energy, 3.36% on average.

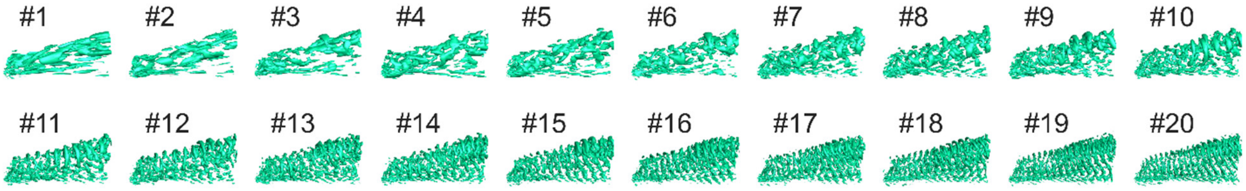

(**a**)

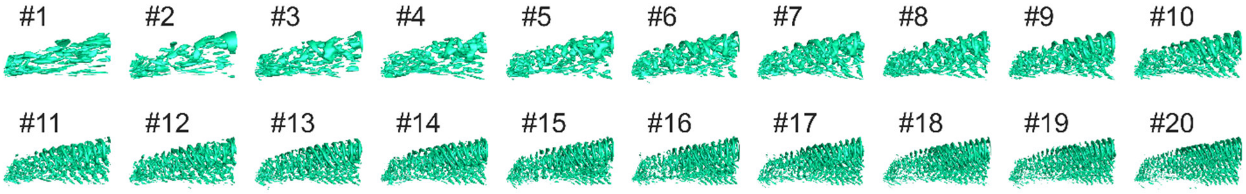

(**b**)

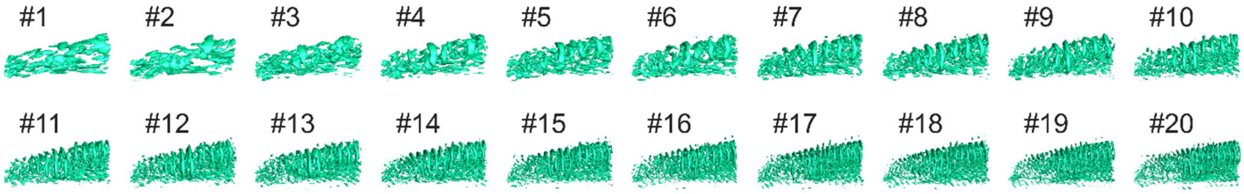

(**c**)

Figure 9. Vortical structures of the first 20 modes behind the MVG with (**a**) Ma 1.5, (**b**) Ma 2.0, (**c**) Ma 2.5.

5.1.3. Mode Time Coefficient and Spectrum Analysis

Figure 10 gives the time coefficients $a(t)$ of the first 20 POD modes in the region behind the MVG for Ma numbers 1.5, 2.0, and 2.5, respectively. It shows that $a(t)$ of the streamwise vortical modes had greater amplitude (138.21 on average), then decreased as the ordinal number increased, resulting in the ring-like vortical modes having smaller amplitude (77.67 on average). Oppositely, as the ordinal number increased, the frequency of $a(t)$ increased in all cases. To investigate the frequency, we performed spectrum analysis for all $a(t)$ signals and found the dominant frequency for each mode. The results are shown in Figure 11. In Figure 11, we observe that different Mach numbers rarely affected the dominant frequency of each mode, and the frequency of ring-like vortical modes (15.54 on average) were higher than the streamwise vortical modes (3.33 on average).

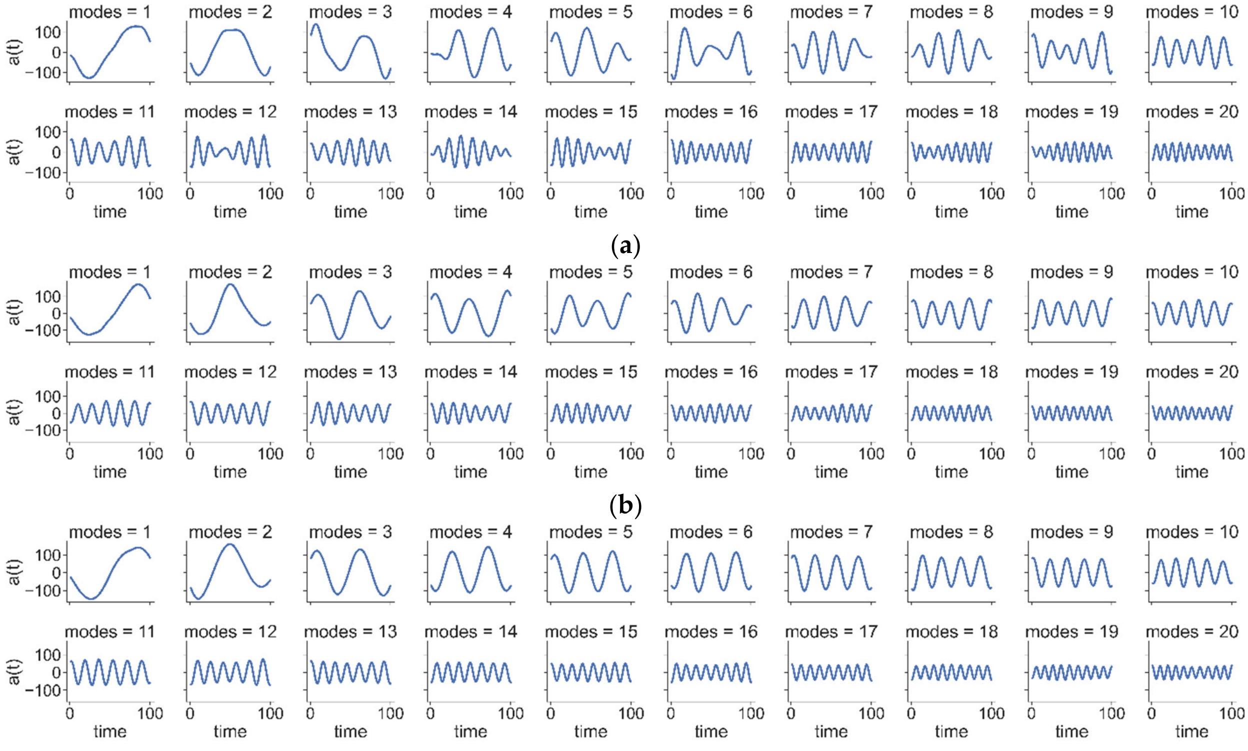

(**a**)

(**b**)

(**c**)

Figure 10. Time coefficients of the first 20 modes behind the MVG with (**a**) Ma = 1.5, (**b**) Ma = 2.0, (**c**) Ma = 2.5.

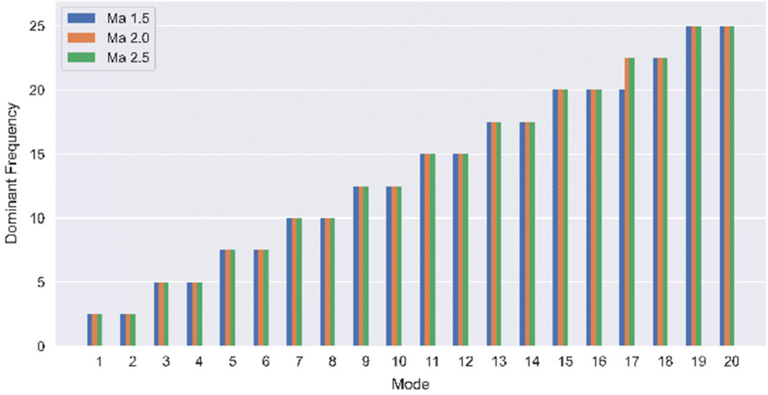

Figure 11. The dominant frequency of the first 20 modes behind the MVG in three different Mach numbers.

5.2. POD Analysis for SWBLI

5.2.1. Mode Energy Distribution

Figure 12 shows $\mathcal{E}(\ell)$ in the SWBLI region in three different Mach numbers. From the distribution of $\mathcal{E}(\ell)$, we also observe that the first 20 modes contained about 98.4, 99.1, and 99.4% of $\mathcal{E}(\ell)$ in the SWBLI region in Mach numbers 1.5, 2.0, and 2.5, respectively. Figure 13 shows the bar plot of the energy percentage of these 20 modes and we could draw the same conclusion with Figure 8, i.e., (1) as the ordinal increases, each mode's contribution rate to the total energy decreases; (2) the energy increases as Mach number increases for the low ordinal modes, but the trend is opposite for the high ordinal modes. In addition, comparing Figures 8 and 13, we could tell that the modes' energy was relatively scattered behind the MVG, but it was concentrated on the lower ordinal modes in the SWBLI region. This was especially distinct for the first mode: the energy percentage was 13~15% in the region behind the MVG and 24~32% in the region of SWBLI, indicating that, as the ring-like vortices travel from the MVG region to the SWBLI region, the low ordinal modes absorb energy from the high ordinal modes.

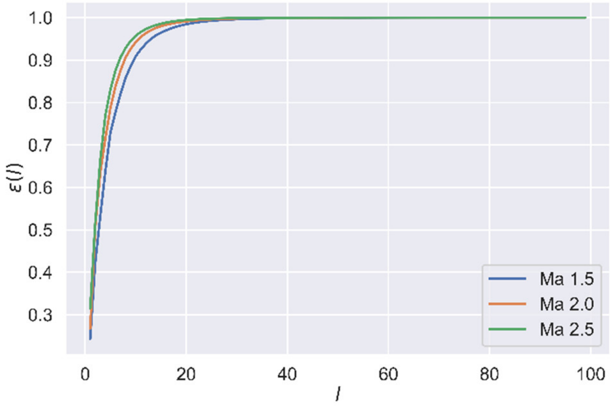

Figure 12. $\mathcal{E}(\ell)$ in the subzone in the SWBLI region in three different Mach numbers.

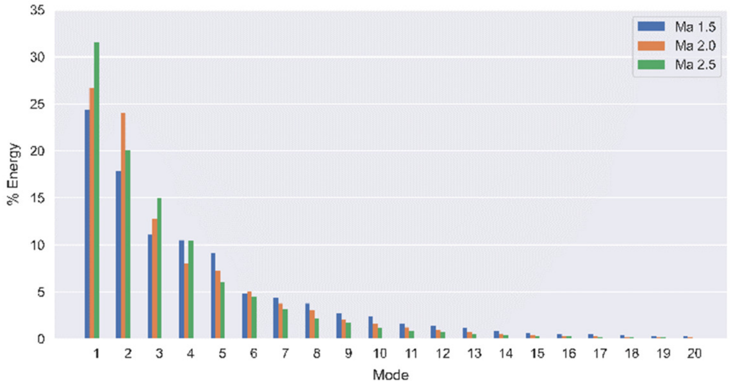

Figure 13. The energy percentage of the first 20 modes in the SWBLI region in three different Mach numbers.

5.2.2. Mode Vortical Structures

Figure 14 shows the vortical structures of the first 20 modes in the SWBLI region with Ma 1.5, Ma 2.0, and Ma 2.5. The vortical structures are also indicated by iso-surfaces of $\|\vec{R}\| = 0.3$. Comparing Figure 14 with Figure 9, we find the conclusions are consistent. The structures of the ring-like vortices were more regular and sturdier. Combining Figures 8, 9, 13 and 14 revealed lower energy levels in the ring-like vortices (2.23%, on average, in the SWBLI region) than streamwise vortices (20.36%, on average, in the SWBLI region), which absorb energy from ring-like vortices as the vortices travel to the SWBLI region. The ring-like vortices had more ordered and sturdy structures and were barely influenced by Mach numbers.

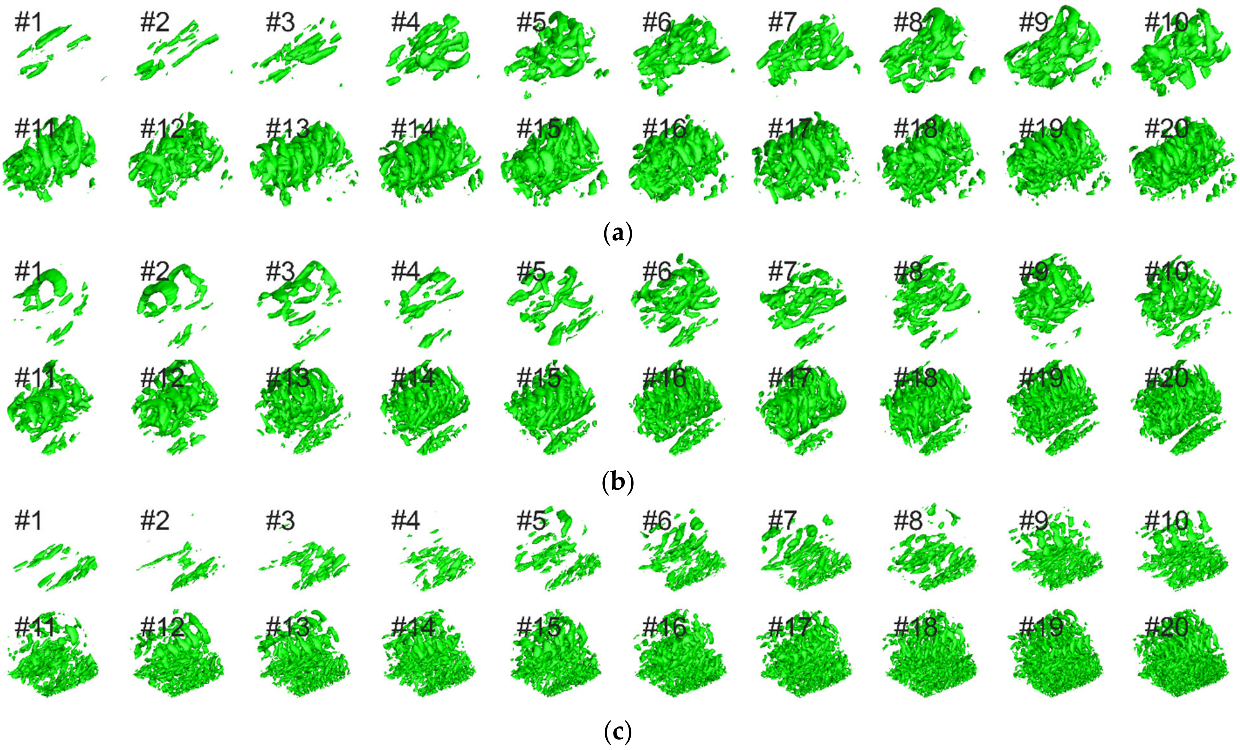

(**a**)

(**b**)

(**c**)

Figure 14. Vortical structures of the first 20 modes in the SWBLI region with (**a**) Ma = 1.5, (**b**) Ma = 2.0, (**c**) Ma = 2.5.

5.2.3. Mode Time Coefficient and Spectrum Analysis

Figure 15 gives the time coefficients $a(t)$ of the first 20 POD modes in the SWBLI region for Ma 1.5, 2.0, and 2.5, respectively. We observed a similar pattern to that in Figure

10, which is that the time coefficients of streamwise vortical modes had greater amplitude (100.28 on average in SWBLI region) and the ring-like ones had smaller amplitude (29.53 on average in SWBLI region). Besides that, there was a difference that was hard to spot between Figure 15 and Figure 10: the amplitude of $a(t)$ in the SWBLI region was relatively smaller than the region behind the MVG, though the frequency seemed consistent. It seems that as the vortices traveled from MVG down to SWBLI region, the vortex intensity was reducing, which could also be observed in the vortical structures, see Figures 9 and 14.

We also performed spectrum analysis and found the dominant frequency for these $a(t)$ signals, see Figure 16. We found similar results with Figure 11, that is, the frequency of the ring-like vortical modes (15.34 on average) were higher than the streamwise modes (3.33 on average). Comparing the same ordinal modes in the region behind the MVG (Figure 11) and the SWBLI region (Figure 16), it is also easy to see the shock wave did not affect the dominant frequency of each mode.

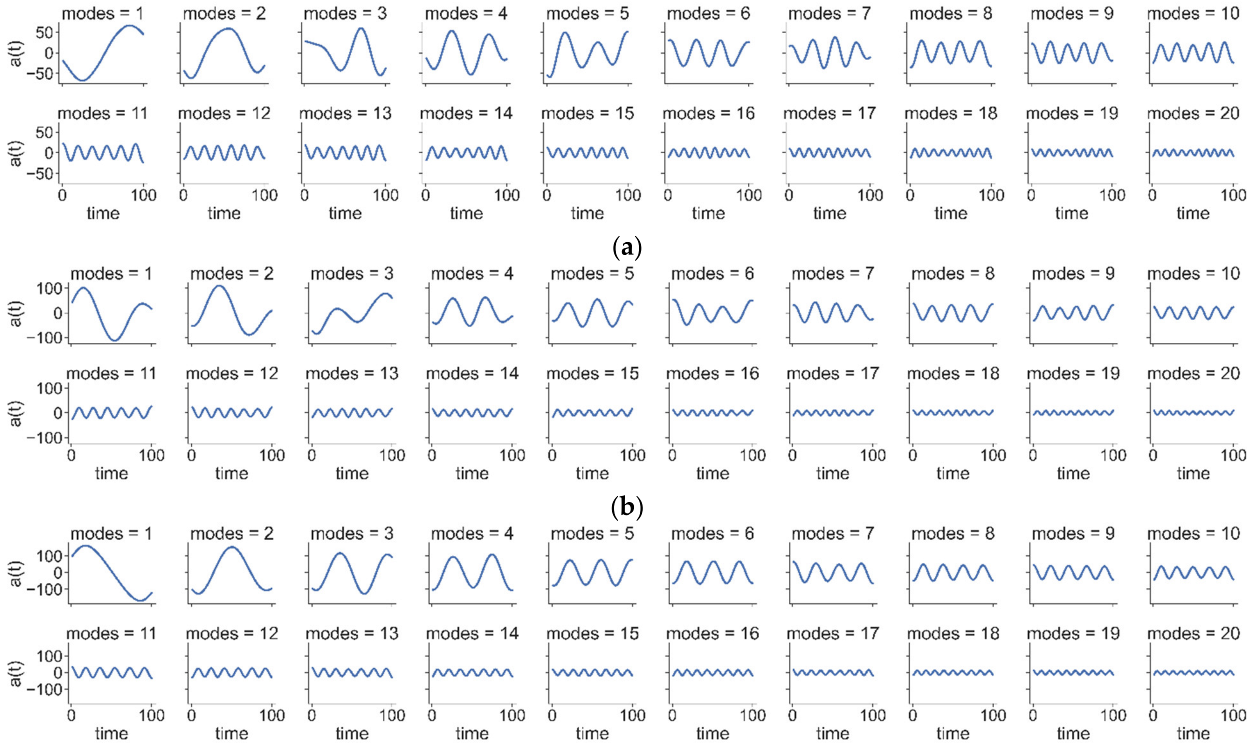

(**a**)

(**b**)

(**c**)

Figure 15. Time coefficients of the first 20 modes in the SWBLI region with (**a**) Ma = 1.5, (**b**) Ma = 2.0, (**c**) Ma = 2.5.

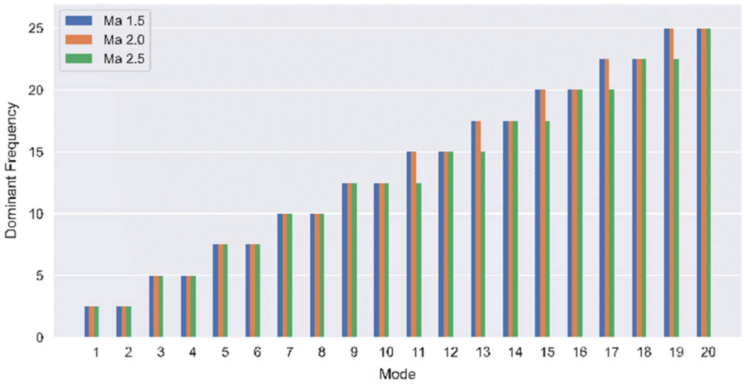

Figure 16. The dominant frequency of the first 20 modes in the SWBLI region in three different Mach numbers.

6. Conclusions

Modal analyses by POD were performed on the vortex structures behind the MVG and in SWBLI region under three different Mach numbers 1.5, 2.0, and 2.5. The numerical results and spectrums suggest that:

1. The streamwise vortical modes and the ring-like vortical modes are disparate in many properties:
    a. The streamwise vortical modes have higher energy (11.83% on average behind MVG and 20.36% in SWBLI region) and the ring-like vortical modes have lower energy (3.36% on average behind MVG and 2.23% in SWBLI region).
    b. The streamwise vortical modes have disordered structure and the ring-like vortical modes have relatively regular structures.
    c. The time coefficients of streamwise vortical modes have greater amplitude (138.21 behind MVG and 100.28 in SWBLI region) and the ring-like ones have smaller amplitude (77.67 behind MVG and 29.53 in SWBLI region).
    d. The frequency of ring-like vortical modes (15.54 on average behind MVG and 15.34 in SWBLI region) are higher than the streamwise modes (3.33 on average behind MVG and in SWBLI region).
2. As Mach number increases:
    a. The energy increases for streamwise vortical modes, and vice versa for ring-like vortical modes;
    b. The structures of streamwise vortical modes are altered significantly, but ring-like vortical modes have robust structures;
    c. The dominant frequency of each mode scarcely varies.
3. As the vortices travel from the MVG down to the SWBLI region:
    a. Streamwise vortices absorb the energy from the ring-like vortices;
    b. The amplitude of the time coefficient decreases;
    c. The dominant frequency of each mode rarely changes.

This suggests ring-like vortices have moderately sturdy structures despite their energies being transferred to streamwise vortices. The independence of each mode's dominant frequency from the Mach numbers and shock waves is also highlighted. The dominant frequency of each mode may depend on the profile of the MVG, which will be investigated in future studies.

Author Contributions: Conceptualization and methodology, Y.Y. (Yong Yang) and Y.Y. (Yonghua Yan); formal analysis, Y.Y. (Yong Yang), Y.Y. (Yonghua Yan), C.C. and Q.W.; writing—original draft preparation, Y.Y. (Yong Yang) and Y.Y. (Yonghua Yan); writing—review and editing, Y.Y. (Yong Yang), Y.Y. (Yonghua Yan), T.A.K. and R.W.; visualization, Y.Y. (Yong Yang), Y.Y. (Yonghua Yan), T.A.K. and R.W. All authors have read and agreed to the published version of the manuscript.

Funding: This research is funded in part by the National Science Foundation's Implementation Grants # 1912191 and 1330801, Mississippi NASA EPSCoR and Mississippi INBRE- funded by an Institutional Development Award from the National Institute of General Medical Sciences of the National Institutes of Health under grant number P20GM103476.

Institutional Review Board Statement: Not applicable.

Informed Consent Statement: Not applicable.

Acknowledgments: This work used the Extreme Science and Engineering Discovery Environment (XSEDE), which is supported by National Science Foundation grant number ACI-1548562.

Conflicts of Interest: The authors declare no conflict of interest.

Nomenclature

MVG	Micro-vortex generator
SWBLI	Shock wave/boundary-layer interaction
DNS	Direct numerical simulation
LES	Large eddy simulation
POD	Proper orthogonal decomposition
Ma	Mach
Re	Reynolds number based on momentum thickness
h	Micro ramp height
x, y, z	Spanwise, normal and streamwise coordinate axes
u, v, w	Spanwise, normal and streamwise velocity

References

1. Ashill, P.R.; Fulker, J.L.; Hackett, K.C. A review of recent developments in flow control. *Aeronaut. J.* **2005**, *109*, 205–232.
2. Babinsky, H.; Li, Y.; Ford, C.P. Microramp control of supersonic oblique shock-wave/boundary-layer interactions. *AIAA J.* **2009**, *47*, 668–675.
3. Dussauge, J.P.; Dupont, P.; Debiève, J.F. Unsteadiness in shock wave boundary layer interaction with separation. *Aerosp. Sci. Technol.* **2006**, *10*, 85–91.
4. Estruch-Samper, D.; Vanstone, L.; Hillier, R.; Ganapathisubramani, B. Micro vortex generator control of axisymmetric high-speed laminar boundary layer separation. *Shock Waves* **2015**, *25*, 521–533.
5. Lin, J.C. Review of research on low-profile vortex generators to control boundary-layer separation. *Prog. Aerosp. Sci.* **2002**, *38*, 389–420.
6. Ma, S.; Chu, W.; Zhang, H.; Li, X.; Kuang, H. A combined application of micro-vortex generator and boundary layer suction in a high load compressor cascade. *Chin. J. Aeronaut.* **2019**, *32*, 1171–1183.
7. Sun, Z.; Scarano, F.; van Oudheusden, B.W.; Schrijer, F.F.; Yan, Y.; Liu, C. Numerical and experimental investigations of the supersonic microramp wake. *AIAA J.* **2014**, *52*, 1518–1527.
8. Wang, Y.; Al-Dujaly, H.; Yan, Y.; Zhao, N.; Liu, C. Physics of multiple level hairpin vortex structures in turbulence. *Sci. China Phys. Mech. Astron.* **2016**, *59*, 624703.
9. Rizzetta, D.P.; Visbal, M.R. Application of large-eddy simulation to supersonic compression ramps. *AIAA J.* **2002**, *40*, 1574–1581.
10. Von Kaenel, R.; Kleiser, L.; Adams, N.A.; Vos, J.B. Large-eddy simulation of shock-turbulence interaction. *AIAA J.* **2004**, *42*, 2516–2528.
11. Ghosh, S.; Choi, J.; Edwards, J.R. RANS and Hybrid LES/RANS Simulations of the Effects of Micro Vortex Generators Using Immersed Boundary Methods. In Proceedings of the 38th Fluid Dynamics Conference and Exhibit, Seattle, WA, USA, 23–26 June 2008; pp. 2008–3726.
12. Lee, S.; Loth, E.; Wang, C. LES of Supersonic Turbulent Boundary Layers with mVG's. In Proceedings of the 25th AIAA Applied Aerodynamics Conference, Miami, Florida, USA, 25–28 June 2007; pp. 2007–3916.
13. Lee, S.; Loth, E. Supersonic Boundary Layer Interactions with Various Micro-Vortex Generator Geometries. In Proceedings of the 39th AIAA Fluid Dynamics Conference, San Antonio, TX, USA, 22–25 June 2009; pp. 2009–3712.
14. John, B.; Emerson, D.R.; Gu, X.J. Parallel Navier–Stokes simulations for high speed compressible flow past arbitrary geometries using FLASH. *Comput. Fluids* **2015**, *110*, 27–35.
15. John, B.; Emerson, D.R.; Gu, X.J. Parallel compressilbe viscous flow simulations using FLASH code: Implementation for arbitrary 3D geometries. *Procedia Eng.* **2013**, *61*, 52–56.
16. Zhang, B.; Zhao, Q.; Xiang, X.; Xu, J. An improved micro-vortex generator in supersonic flows. *Aerosp. Sci. Technol.* **2015**, *47*, 210–215.
17. Said, I.; Poonaesparan, M.K.; Bohari, B.; Idiris, A.C.; Rahman MR, A.; Saad, M. The Effect of Streamwise Location of Micro Vortex Generator on Airfoil Aerodynamic Performance in Subsonic Flow. *J. Aeronaut. Astronaut. Aviat.* **2020**, *53*, P173–178.
18. Khare, A.; Khurana, S. Effect of Micro Vortex Generator Width on Vortex Characteristics. In Proceedings of the AIAA Aviation 2022 Forum, Chicago, IL, USA, 27 June–1 July 2022; pp. 2022–3388.
19. Yan, Y.; Yang, Y.; Chen, C.; Cotton, H.A.; Serrano, A. Numerical study on the ring-like vortex structure generated by MVG in high-speed flows with different Mach numbers. *Jpn. J. Ind. Appl. Math.* **2022**, *39*, 3–18.
20. Yan, Y.; Chen, L.; Li, Q.; Liu, C. Numerical study on microramp vortex generation for supersonic ramp flow control at Mach 2.5. *Shock Waves* **2016**, *27*, 79–96.
21. Yang, Y.; Yan, Y.; Liu, C. ILES for mechanism of ramp-type MVG reducing shock induced flow separation. *Sci. China Phys. Mech. Astron.* **2016**, *59*, 1–12.
22. Volkwein, S. *Proper Orthogonal Decomposition: Theory and Reduced-Order Modelling*; University of Konstanz: Konstanz, Germany, 2013.
23. Martın, M.P.; Taylor, E.M.; Wu, M.; Weirs, V.G. A bandwidth-optimized WENO scheme for the effective direct numerical simulation of compressible turbulence. *J. Comput. Phys.* **2006**, *220*, 270–289.

24. Adams, N.A. Direct simulation of the turbulent boundary layer along a compression ramp at M = 3 and Req = 1685. *J. Fluid Mech.* **2000**, *420*, 47–83.
25. Yan, Y.; Tang, J.; Liu, C.; Yang, F. DNS study on the formation of Lambda rotational core and the role of TS wave in boundary layer transition. *J. Turbul.* **2016**, *17*, 572–601.
26. Liu, C.; Gao, Y.S.; Dong, X.R.; Wang, Y.Q.; Liu, J.M.; Zhang, Y.N.; Cai, X.S.; Gui, N. Third generation of vortex identification methods: Omega and Liutex/Rortex based systems. *J. Hydrodyn.* **2019**, *31*, 774–781.